OPEN ACCESS
Modern Physics Letters B
Vol. 36, No. 15 (2022) 2241002 (15 pages)

DOI: 10.1142/S0217984922410020

Time-frequency analysis of venous pulsatile flow and sigmoid sinus vascular wall displacement causing pulsatile tinnitus using time series and magnitude squared coherence methods

Yue-Lin Hsieh†

Department of Otology and Skull Base Surgery, Eye Ear Nose & Throat Hospital, Fudan University, Shanghai 200031, China

NHC Key Laboratory of Hearing Medicine, Shanghai 200031, China
tb22521208@hotmail.com

Yue-Da Hsieh†

Department of Economics, London School of Economics and Political Science, London WC2A 2AE, UK
y.hsieh@lse.ac.uk

Wuqing Wang*

Department of Otology and Skull Base Surgery, Eye Ear Nose & Throat Hospital, Fudan University, Shanghai 200031, China.

NHC Key Laboratory of Hearing Medicine, Shanghai 200031, China
wwuqing@eent.shmu.edu.cn

Received 2 November 2021
Revised 4 February 2022
Accepted 19 February 2022
Published 25 May 2022

Displacement of the sigmoid sinus vascular wall and intrasinus blood flow motion is known to cause pulsatile tinnitus (PT) in patients with sigmoid plate dehiscence. To investigate the source of sound that causes PT, this study sought to determine the correlation between *in vivo* displacement of the vascular wall and intrasinus flow hemodynamics. A confocal laser displacement sensor and color-coded Doppler ultrasound system were implemented on a participant diagnosed with venous PT. The displacement and

*Corresponding author.

†Co-first authors.

Doppler velocity data were analyzed using time series and magnitude squared coherence methods. The median and peak displacement values of the vascular wall were 6.7 μm and 11.7 μm, respectively. The major frequency range of vascular displacement was below 4 Hz. The portmanteau test was rejected for different values of m. The cross-correlation of the two processes was not zero, indicating the existence of cross-correlation. The peak magnitude squared coherence of the two gauged signals was 0.3 at 7.143 Hz. The displacement of the sigmoid sinus vascular wall was temporally correlated with the intrasinus flow, although the major frequency range of the induced vascular displacement fell below the human hearing threshold. Therefore, the hydroacoustic and vibroacoustic sounds induced by the fluid–structure interaction between the vascular and osseous structures overweighed the displacement of the vascular wall at the focal dehiscence area in PT production.

Keywords: Pulsatile tinnitus; vascular displacement; venous flow; time series; magnitude squared coherence.

1. Introduction

Vascular pulsatile tinnitus (PT) is an abnormal sensation of the vascular sound and/or forced vibroacoustic sound induced by the impact of blood flow.[1,2] Among different vascular origins, venous PT comprises the largest demographic.[3] Sigmoid sinus wall anomalies (SSWAs) consist of sigmoid sinus wall dehiscence and diverticulum and are the most well-studied anatomical anomalies in patients with venous PT.[4] Although the clinical management of SSWAs has been well documented in the literature,[3,5] the underlying mechanisms of PT remain unknown.

Most clinical studies have postulated that PT is caused by hydroacoustic and/or vibroacoustic noises.[6,7] During cardiac diastole, the positive intracranial pressure gradient and downstream negative intravenous pressure facilitate the return of sinus flow to the right atrium.[6] The hydroacoustic noise arises from the turbulent blood flow and fluctuation of flow pressure gradient inside the dural venous sinus.[6] Conversely, in patients with dehiscence, the pressure exerted on the vascular wall (causing focal vascular displacement due to the absence of overlying sigmoid plate) triggered by the pulsing blood flow generates the forced vibroacoustic sound.[8–12] Although the displacement of the sigmoid sinus vascular wall at the focal dehiscent area produces pulse-synchronous sounds has been debatable,[13,14] a thin layer of bone plate overlying the surface of the sigmoid sinus vascular wall has been identified in patients with dehiscence predetermined via traditional CT scans during intraoperative observation.[13] This thin layer of the bone plate is tightly fixated on the surrounding bone tissues with a sheet of layers of dura mater underneath.[13] Omitting the thinned tissue of the sigmoid plate and dura mater overlying the sigmoid sinus vessel wall can cause experimental bias and false interpretation of the displacement data. Thus, a battery of *in vivo* sensing applications and microstructural studies is needed to verify the notion that the vibration of the sigmoid sinus vascular wall induces PT.

As the vibroacoustic sound is potentially the more dominant source of PT reckoned by recent computational and experimental studies,[12,15,16] this study focused on the time-frequency correlation between pulsing sinus flow and the displacement

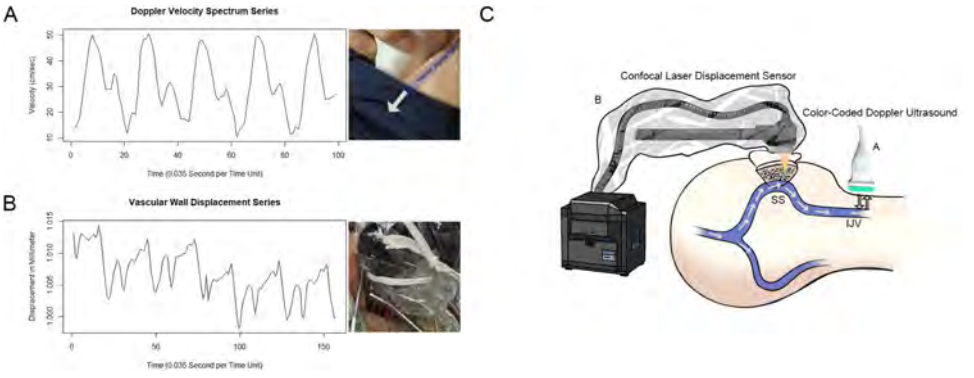

Fig. 1. (Color online) *In vivo* experimental setup using intraoperative confocal laser displacement sensor and color-coded Doppler ultrasound. SS: sigmoid sinus, IJV: internal jugular vein. (A) The intrasinus velocity spectrum detected by the Doppler system. (B) The displacement data of the sigmoid sinus vascular wall obtained using a portable confocal laser displacement sensor.

of the sigmoid sinus vascular wall. The correlation between the *in vivo* gauged intravascular flow and displacement of the sigmoid sinus vascular wall was assessed using bioinformatics and statistical analyses. Knowledge of the time-frequency correlation between vascular wall displacement and flow velocity pulsation merits an understanding of the vibroacoustic mechanism of PT, which can facilitate further development of the transtemporal surgical techniques.

2. Methods

2.1. *In vivo vascular displacement/flow velocity data acquisition and patient data*

To evaluate the vibration of the vascular wall, a confocal multicolor laser displacement sensor system CL-P030N (Keyence, Japan) with 0.25 μm resolution and high-precision linear measurement range ± 0.72 μm was implemented in this study. The setup of a confocal multicolor laser displacement was previously introduced.[13,14] A sterile sleeve was used to cover the IP67 waterproof laser sensor head and the stand placed near the surgeons. The sensor head was later exposed and disinfected using a 2.5% iodine tincture followed by 75% alcohol for deiodination. After sterilization, the sensor head was aligned perpendicular to the prominent region of the sigmoid sinus vascular surface. The operative techniques to expose the surface of the sigmoid sinus wall and methods of sensing angulations were previously introduced. The sampling cycle was set to 1000 μs. CL-NavigatorN 1.4.0.0 (Keyence, Japan) was used to obtain the displacement data. The vascular displacement data were collected after the removal of the dehiscent bone plate.

The measurement of jugular flow was described in our previous study.[7] To acquire the flow velocity data of the upper neck, a color-coded Doppler ultrasonographic system (MyLabTM ClassC; Esoate SpA, Genoa, Italy) was used.

The time units are interpolated for the purpose of performing statistical analysis uniformly. An interpolation method was used to unify the time units of the obtained vascular displacement (157 time points) and flow velocity data (99 time points; 0.035 s per time point). Figure 1 shows the *in vivo* sensed data used for the bioinformatics investigations.

The participant was a 25-year-old woman with right-sided venous PT. The PT disappeared during internal jugular vein compression. Sigmoid sinus wall dehiscence and transverse-sigmoid sinus enlargement were detected on the PT side using high-resolution temporal CT and magnetic resonance venography. After meticulous examinations, extraluminal sigmoid sinus angioplasty was performed in December 2020, with a follow-up duration of 10 months. The surgical technique was previously described.[7,17,18] The loudness of the PT was reduced from 8 to 3 using the visual analog scale after the operation. The participant provided written informed consent. The experimental measurements were conducted in accordance with the principles of the Declaration of Helsinki. Ethics approval was obtained from the Ethical Committee of the Eye, Ear, Nose, and Throat Hospital in Shanghai, China.

2.2. *Time-series analysis*

Time series analysis is a common method for analyzing a sequence of random variables given a time domain. In this study, both multivariate and univariate time-series models were used to assess the two stochastic processes, namely, displacement of the vascular surface and velocity spectrum.

Multivariate time-series analyses were used to assess the statistical relationships between the two processes. A zero cross-correlation test or multivariate Portmanteau test ($p > 0.05$) was performed on the two series (Eq. (1)). Formally,

$$Q_k(m) = T^2 \sum_{l=1}^{m} \frac{1}{T-l} \hat{b}_l' (\hat{\rho}_0^{-1} \otimes \hat{\rho}_0^{-1}) \hat{b}_l, \tag{1}$$

where $\hat{b}_l = \mathrm{vec}(\hat{\rho}_l')$ and $\otimes =$ the Kronecker product of two matrices.

Univariate time series models were used to represent stochastic processes of the displacement of the vascular surface and velocity spectrum to evaluate their ideocracies. The class of time series model used in our analysis was based on linear time series models, namely, (multiplicative seasonal) autoregressive integrated moving average (ARIMA) models.

The modeling procedure involved five steps: (1) analysis of the time series and linear models, (2) identification and selection of the best model fit for the time series, (3) parameter estimation using maximum likelihood methods of the selected model, (4) validation of the model, and (5) future predictions of the linear time series to determine how well the model is fitted by model backtesting.

First, Jarque–Bera normality tests were performed to assess the distribution of the displacement of the vascular surface and velocity spectrum processes. This test was conducted to confirm whether the distributions of the stochastic processes

were asymptotically normally distributed, ultimately facilitating the backtesting and parameter fixing of the time series modeling to ensure the soundness of our analyses. To ensure that the stochastic processes were stationary, the Phillips–Perron test was performed to confirm the unit-root stationarity of the process. Because these models capture statistical dependencies in a stochastic process, the Ljung–Box test was performed to assess the autocorrelation within a process. The test was also applied to the residuals of the series, thereby ensuring the appropriateness of the model fitting.

For model selection, methods of the sample autocorrelation function/partial autocorrelation function, extended autocorrelation function (EACF), and Akaike information criterion (AIC) were used. The final model was selected based on minimal AIC. To interpret the results, a backshift operator was introduced:

$$B(x_t) = B * x_t := x_{t-1}, \quad \text{with } B(c) := c \quad \text{for all } c \in \mathbb{R}. \tag{2}$$

Of note, a general ARIMA(p, d, q) model defined by the backshift operator is as follows:

$$\phi(B)r_t = \phi_0 + \theta(B)a_t, \tag{3}$$

where t is the index time, r_t is the response series at time t, d is the amount of first-order difference, ϕ_0 is the drift constant that shifts the process parallelly, and $\phi(B)$ is the autoregressive (AR) operator. A p-order polynomial in the backshift operator is characterized by $\phi(B) = 1-\phi_1(B)-\cdots-\phi_p(B)^p$, where $\theta(B)$ is the moving-average (MA) operator. A q-order polynomial in the backshift operator is characterized by $\theta(B) = 1 - \theta_1(B) - \cdots - \theta_q(B)^q$. a_t is the independent and identically distributed innovation, sometimes called shock at time t, which is a white noise.

An ARIMA model is a collection of linear combinations of r_t's past values $\phi(B)r_t$ and a linear combination of previous shocks $\theta(B)a_t$. A general multiplicative seasonal ARIMA(p, d, q)(P,D,Q)$_S$ defined by the backshift operator is $\phi(B)\Phi(B^S)(1-B)^d(1-B^S)^D r_t = \phi_0 + \theta(B)\Theta(B^S)a_t$, where $\Phi(B^S) = 1 - \Phi_1 B^S - \cdots - \Phi_P(B)^{\mathrm{PS}}$; $\Theta(B^S) = 1 - \Theta_1 B^S - \cdots - \Theta_P(B)^{\mathrm{PS}}$. All other parameters are equally defined in the ARIMA(p, d, q) models.

2.3. *Magnitude squared coherence*

The magnitude squared coherence estimate is a frequency function (Eq. (4)), with values between 0 and 1. These values signify the strength of the correlation between x and y at each frequency. The equation is as follows:

$$C_{xy}(f) = \frac{|P_{xy}(f)|^2}{P_{xx}(f)P_{yy}(f)}, \tag{4}$$

where $P_{xx}(f)$ and $P_{yy}(f)$ represent the power spectral densities and $P_{xy}(f)$ of x and y is the cross-power spectral densities.

In multiinput and output systems, the formula is restructured as follows:

$$C_{X_{y_i}}(f) = \frac{P^{\dagger}_{X_{y_i}}(f) P^{-1}_{XX}(f) P_{X_{y_i}}(f)}{P_{y_i y_i}(f)}$$

$$= [P^{*}_{x_1 y_i}(f) \cdots P^{*}_{x_m y_i}(f)] \begin{bmatrix} P_{x_1 x_1}(f) & P_{x_1 x_2}(f) & \cdots & P_{x_1 x_m}(f) \\ P_{x_1 x_1}(f) & P_{x_2 x_2}(f) & \cdots & P_{x_2 x_m}(f) \\ \vdots & \vdots & \ddots & \vdots \\ P_{x_m x_1}(f) & P_{x_m x_2}(f) & \cdots & P_{x_m x_m}(f) \end{bmatrix}$$

$$\times \begin{bmatrix} P_{x_1 y_i}(f) \\ \vdots \\ P_{x_m y_i}(f) \end{bmatrix} \frac{1}{P_{y_i y_i}(f)}, \tag{5}$$

where X is the array of m inputs; $P_{X_{y_i}}$ is the m-dimensional vector of cross-power spectral densities between inputs, y_i; P_{XX} is the cross-power spectral of inputs, the m-by-m matrix of power spectral densities; $P_{y_i y_i}$ is the power spectral density of the output; and the dagger (†) is the complex transpose of conjugate.

2.4. *Spectrotemporal analyses*

To demonstrate the spectrotemporal characteristics of the measured displacement, discrete Fourier transform (DFT), short-time Fourier transform (STFT), continuous wavelet transformation (CWT), and variation mode decomposition (VMD) methods were implemented using MATLAB R2017a (MathWorks).

The DFT (Eq. (1)) is a useful discrete transformation used to perform Fourier analysis in many practical applications. DFT transforms a sequence of N complex numbers into another. The DFT formulation is defined by

$$x_n = \sum_{k=0}^{N-1} X_k e^{i\frac{2\pi}{N}kn} \quad n = 0, \ldots, N-1, \tag{6}$$

where X_k indicates Fourier amplitude.

Owing to the pulsatile nature of PT, discrete STFT facilitates the determination of the chunked magnitude and phase for each point in time and frequency. The original formulation of the continuous STFT is reformulated to a discrete form as follows:

$$\mathrm{STFT}\{x[n]\}(m, \omega) \equiv X(\tau, \omega) = \sum_{n=-\infty}^{\infty} x[n] w[n-m] e^{-j\omega n}, \tag{7}$$

where $x[n]$ represents the sequence of discretized time-domain signals to be transformed, m is the time index, ω is the frequency, and $w[n]$ denotes the sequence of the discretized window functions.

The CWT (Eq. (8)) is a mathematical method that improves the non-stationary signals and identifies the echoes representing defects, which allows the translation and scale parameter of the wavelets to continuously alter:

$$X_w(a,b) = \frac{1}{|a|^{1/2}} \int_{-\infty}^{\infty} x(t)\bar{\psi}\left(\frac{t-b}{a}\right) dt, \tag{8}$$

where $\psi(t)$ is a continuous function in the time and frequency domains.

The VMD decomposed (Eq. (9)) input signals into discrete sub-signals that enhance the resolution of data visualization:

$$\min_{\{u_k\},\{\omega_k\}} \left\{ \sum_k \left\| \partial_t \left[\left(\delta(t) + \frac{j}{\pi t}\right) * u_k(t) \right] e^{-j\omega_k t} \right\|_2^2 \right\},$$
$$\text{s.t.} \quad \sum_k u_k = f, \tag{9}$$

where $\{u_k\} := \{u_1, \ldots, u_K\}$ and $\{\omega_k\} := \omega_1, \ldots, \omega_K$ are shorthand notations of the entire modes and their center frequencies and $\sum := \sum_{k=1}^{K}$ is the aggregation over all nodes. The moderate bandwidth constraint alpha = 2000, tau = zero, three modes $k = 5$, DC = zero, and initialized omega was uniform (initialization set at 1).

2.5. *Microstructure observation of the dehiscent sigmoid plate*

The dehiscent sigmoid plate was harvested during the transtemporal osteovascular reconstruction surgery. The specimen was immediately immersed in a fixative, 4% paraformaldehyde solution, for 24 h and 75% alcohol for dehydration. An ultra-high-resolution field-emission scanning electron microscope (SEM) Regulus8100 (HITACHI, Japan) at 3.0 kV was used to observe the harvested dehiscent sigmoid plate.

3. Results

3.1. *Sigmoid plate displacement and Doppler flow characteristics*

The displacement and flow characteristics are given in Table 1. The median displacement of the sigmoid sinus vascular wall was 0.006736 mm (0.003936/0.008836 mm). The largest displacement within the pulsatory cycle was 0.0117 mm. The median flow velocity of the velocity spectrum was 28.6 (21.8/40.3) cm/s. The peak fluctuation of the flow velocity was 39.3 cm/s.

Table 1. Sigmoid sinus vascular wall displacement and Doppler velocity data.

	Displacement of vascular surface (mm)	Doppler velocity (cm/s)
Median	0.006736 (0.003936/0.008836)	28.6 (21.8/40.3)
Peak variation	0.0117	39.3

3.2. *Time series analysis*

A multivariate Portmanteau test was applied to the two combined processes. Based on the results, a linear dynamic dependence existed between the processes as the null of the multivariate Portmanteau test was rejected at different values of m. The cross-correlation of the two processes was not zero, indicating that the displacement of the vascular surface and the flow velocity spectrum were cross-correlated. Both processes were found to be suitable for model fitting as the results of the Ljung–Box test were $p < 0.01$ for both (Table 2).

The linear time series ARIMA model was used to study the linear pattern in the series of displacements of the vascular surface and velocity spectrum. Jarque–Bera normality tests with quantile and quantile–quantile (Q–Q) plots were applied to the two processes and suggested that both series were normally distributed, with p-values of 0.4338 and 0.0655 (Table 3). As both series were normally distributed, the interval estimation and model parameter fixing depending on its significance were set to 1.96 with 95% significance. In addition, the Phillips–Perron test showed that the two series were not unit-root non-stationary, as the null hypothesis of the test was rejected for both series (Table 4).

Owing to the normalization of time, the displacement of the vascular surface and velocity spectrum exhibited different linear structures. The model estimation results are shown in Tables 5 and 6. As both processes were asymptotically normal, the model fix of standard error with respect to its coefficient estimates was applied to both models. The coefficient estimates $\hat{\phi}_{i_{\mathrm{MLE}}}$ are insignificant (fixed to 0) at the chosen significance level if and only if $|\hat{\phi}_{i_{\mathrm{MLE}}}| < 1.96|$ s.e. $(\hat{\phi}_i)|$.

To validate the model, the Ljung–Box test was applied to the model residual series. The residuals of the two series were white noises, as the test results were

Table 2. Autocorrelation analysis.

Ljung–Box test	Test statistics: Chi-Squared	p-value
Displacement of vascular surface	320.42	p-value < 2.2e–16
Velocity spectrum	133.47	p-value < 2.2e–16

Table 3. Results of the normality tests.

Jarque–Bera normality test	Test statistics: Chi-Squared	p-value
Displacement of vascular surface	1.6704	0.4338
Velocity spectrum	5.4516	0.06549

Table 4. Results of the test for unit-root.

Phillips–Perron test	Z_rho (lag)	p-value
Displacement of vascular surface	−32.4 (3)	p-value < 0.01
Velocity spectrum	−24.2	0.0229

Table 5. Analysis of sigmoid sinus vascular wall displacement using the ARIMA model.

Displacement of vascular surface		Model: SARIMA(25,0,0)(5,0,0)		
Parameters	Estimates (Standard Error)	Log likelihood	AIC	Lagged
AR 5	0.6866 (0.0660)	688.13	−1362.25	5
AR 14	−0.2329 (0.0820)			14
AR 19	0.2363 (0.0897)			19
AR 23	0.1941 (0.0721)			23
SAR 5	−0.4341 (0.0833)			Seasonal 5
Intercept	1.007 (0.001)			Intercept

Table 6. Analysis of Doppler velocity spectrum using the ARIMA model.

Velocity spectrum		Model: SARIMA(23,0,0)(2,0,0)		
Parameters	Estimates (Standard Errors)	Log likelihood	AIC	Lagged
AR 1	−0.3667 (0.1368)	−224.73	469.46	1
AR 2	−0.4063 (0.1096)			2
AR 20	0.4903 (0.0678)			20
AR 21	0.5759 (0.0957)			21
AR 22	0.4277 (0.1096)			22
AR 23	0.2531 (0.0887)			23
SAR 1	1.3063 (0.1396)			Seasonal 1
SAR 2	−0.5197 (0.1326)			Seasonal 2
Intercept	29.4153 (7.1535)			Intercept

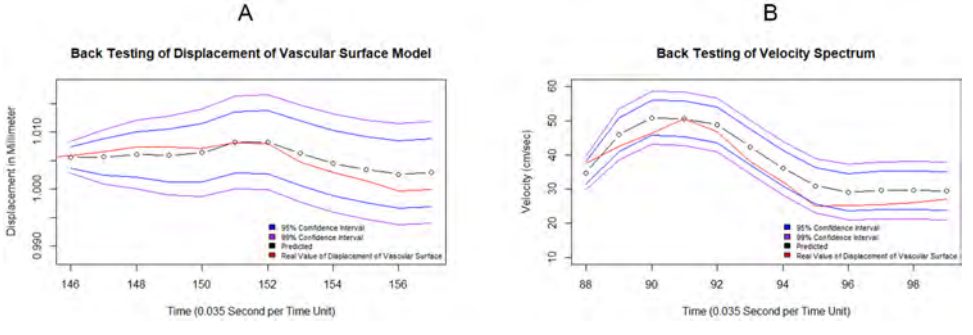

Fig. 2. (Color online) Backtesting of the two series. (A) Backtesting of the displacement of vascular surface and (B) Doppler velocity of one pulsatory cycle.

$p = 0.999$ for the displacement of the vascular surface and $p = 0.993$ for the velocity spectrum. These results imply that the models for the two processes were adequately fitted. In addition, time-series backtesting was performed by first reducing the series by 12 time points (validation sample) and then using the selected model to forecast 12 points for comparison with the 12 validation sample points (Fig. 2).

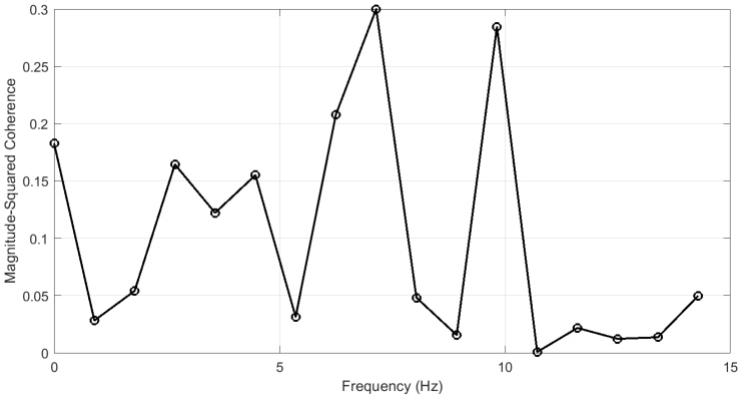

Fig. 3. Frequency analysis using the magnitude squared coherence method.

3.3. *Magnitude squared coherence analysis*

In the frequency correlation analysis, the magnitude squared coherence method revealed that the displacement of the sigmoid sinus vascular wall in the frequency range of 5–10 Hz was most correlated with that of the intrasinus blood flow detected by Doppler ultrasound (Fig. 3). The correlation between the two signals was 0.3 at a frequency of 7.143 Hz. No overlapping frequency was observed between the two selected signals. As the intrasinus blood flow velocity fluctuates due to negative pressure during the heart diastole, the frequency of 7.143 Hz did not correspond to the participant's heart rate (81 beats per minute). Influencing factors that cause flow phases were the motions of the working valves, such as the jugular and tricuspid valves. In addition, according to the spectrotemporal analysis, the displacement frequency of the sigmoid sinus vascular wall above 6 Hz was significantly reduced. The coherence of both signals above a frequency of 10.71 Hz was below 0.1. The peak coherence ratio of the two investigated signals was less than or equal to 0.3.

3.4. *Bioinformatic analysis*

Figure 4 shows a visual of the gauged sigmoid sinus wall displacement. In Fig. 4(A), owing to the restriction of the sampling rate, only the frequency range below 14 Hz is displayed. The amplitude of the displacement markedly declined above 6 Hz and was at least two times lower than that observed at frequencies below 4 Hz. By displaying the spectrotemporal results, Figs. 4(B)–4(D) indicate that the major frequency of the vascular wall displacement amplitude was below 4 Hz, with recognizable pulse-synchronous patterns. However, low-amplitude signals above 4 Hz were present, despite a significant reduction in the amplitude.

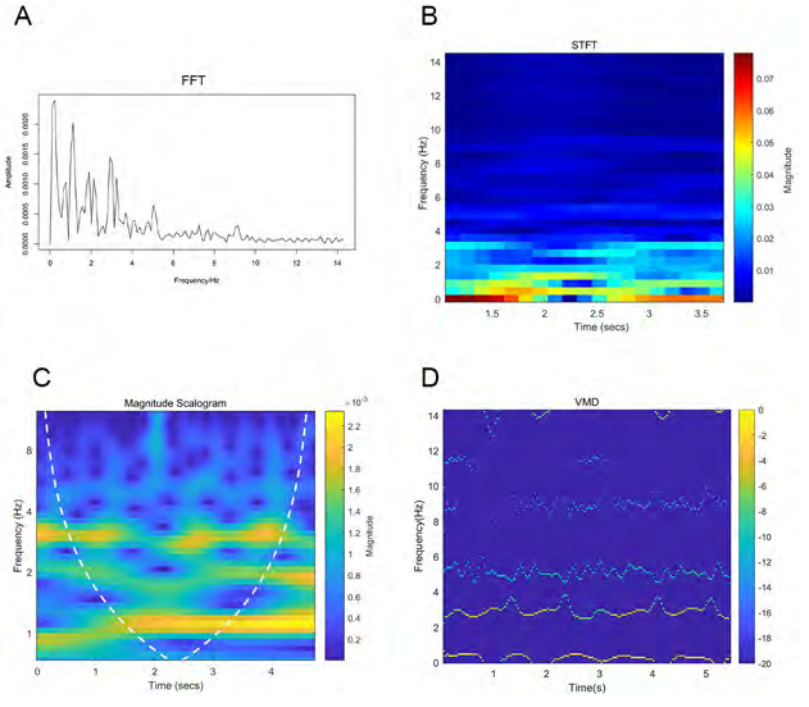

Fig. 4. (Color online) Time-frequency results of sigmoid sinus vascular wall displacement displayed in (A) Fast Fourier transform, (B) STFT, (C) continuous wavelet, and (D) variational mode decomposition.

4. Discussion

In this study, we analyzed the correlation between the *in vivo* sensed vascular wall displacement and flow velocity using time series and magnitude squared coherence methods. The results suggest that a temporal correlation exists between the motion of the blood flow and displacement of the sinus wall. This finding highlights the importance of evaluating the pulse-synchronicity of patients' tinnitus to correctly differentiate the vascular origin of PT. As venous PT instantaneously pauses by applying digital compression over the ipsilateral internal jugular vein, displacement of the dehiscent vascular wall is highly related to intravascular hemodynamics. However, the major frequency of sensed displacement was low and fell below the human hearing threshold. Such finding indicates that based on the current sensing application, the vascular wall displacement above 0.72 μm within 0.001 s may not be a major factor that causes PT. As the displacement of the vascular wall is compliant with the fluctuation of velocity and wall pressure,[11] and the venous flow velocity is a double-humped wave, the amplitude of vascular displacement above 4 Hz significantly declines. Although it is unknown whether subtle vibrations below 0.72 μm of

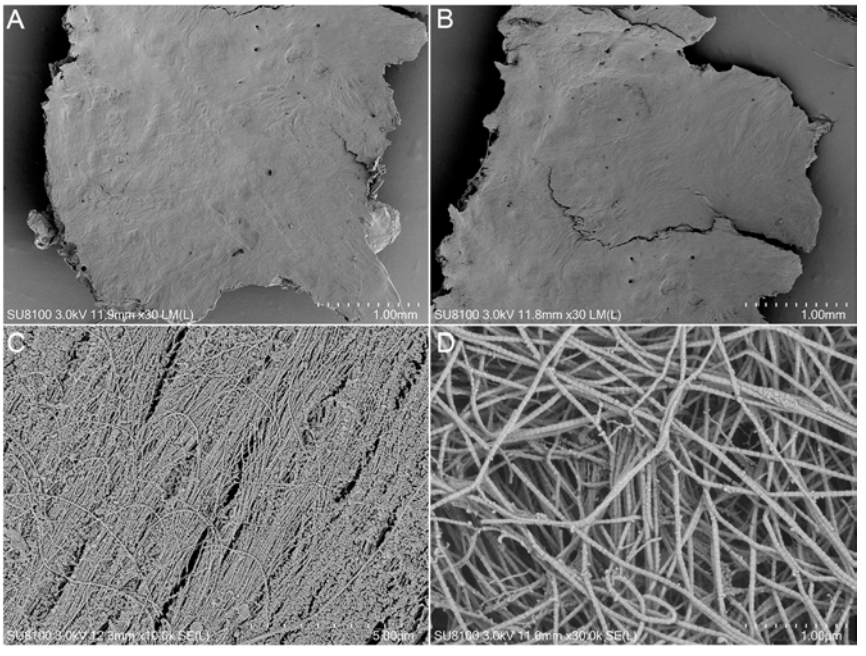

Fig. 5. SEM photographs of the dehiscent sigmoid plate (magnification 30×). (A) The convex surface of the harvested dehiscent sigmoid plate (magnification 30×). (B) The concave surface of the harvested dehiscent sigmoid plate (magnification 30×). (C) The concave surface of the harvested dehiscent sigmoid plate and collagen fibers of dura mater (magnification 10,000×). (D) Collagen fibers of dura mater overlying the concave surface of the dehiscent sigmoid plate (magnification 30,000×).

the sigmoid sinus vascular wall cause audible noise, a thinned piece of translucent bone plate overlying the dehiscent region overlies the vascular surface. Additionally, layers of the dura mater fixate tightly between the sigmoid plate and vascular wall (Fig. 5). Collectively, these structures reduce the displacement of the vascular walls. Hence, besides the air-conduction transmission pathway, sound-induced by fluid–structure interaction may also be transmitted via the bone conduction route.[19,20]

Recent numerical studies have demonstrated that as per computational results, the peak displacement of the vascular wall reaches 8 μm, causing 75.16 dB vibroacoustic noise at 1200 Hz.[12] Despite a significant difference between *in vivo* and computational frequency,[12–15] high computational frequency might be due to the morphological changes caused by oscillation of the inner vascular surface elicited from the flow impact. However, the displacement sensor only measures the outer surface displacement of the vascular wall. The compliance and morphological compression of the vascular wall induced by the flow-exerted wall pressure may markedly impact the frequency outcome. Thus, the current displacement sensor detected a peak displacement above 11 μm after the vascular wall was separated from the sigmoid wall. As the establishment of the overlying dehiscent sigmoid plate and dura

mater can be arduous in numerical studies, and *in vivo* studies have demonstrated a significant difference between the separation of the dehiscent bone plate from the vascular wall,[13,14] the vibroacoustic sound source may not arise from the bulk displacement of the vascular wall at the focal dehiscent area alone. This finding is consistent with our recent coupled CFD study, which suggests that the forced vibration of juxta-dehiscent osseous and vascular tissues, as a source, causes PT.[13] Thus, computational investigations of the vibration of the sigmoid sinus vascular wall or the entire transverse-sigmoid sinus that produces PT are warranted. Furthermore, our previous intraoperative findings highlighted that precluding the displacement of the vasculature using rigid auricular cartilage was insufficient to eliminate PT in some patients.[17] In addition to the generation of vibroacoustic sound, pressure changes in the middle ear cavity may affect the aerial volume and pressure inside the mastoid cavity, causing movements of the tympanic membrane and/or the ossicular chain.[7,21] Therefore, an investigation of the energy transmittance of vascular displacement inside the middle ear is warranted.

The hydroacoustic sound generated by vortex and fluctuation of the flow pressure gradient is another major source of PT. In previous *in vitro* studies, flow sounds produced using 3D-printed models or CFD caused spectrotemporal results similar to those recorded using the *in vivo* trans-canal recording technique.[6,16,22] In addition, the flow sound could be recorded using a stethoscope placed at the outer surface of the 3D-printed vascular wall,[23] suggesting that the influence of hydroacoustic sound should not be neglected. By excluding the vascular displacement, the Doppler recording technique revealed that the flow sound shares comparable spectrotemporal characteristics.[20] These findings indicate that the intrasinus flow can be a predominant factor causing PT. Because the major frequency of the generated flow sound fluctuates below 500 Hz, the 1/3 octave narrow band noise at the center frequency of 125/250/500 Hz from an audiometer can match patients' perception of PT.[6,20] Based on previous clinical and experimental studies, patients with venous PT may perceive both vibroacoustic and hydroacoustic sounds.[12,13]

This study had several limitations. First, acquiring displacement data below 0.72 μm are currently impossible owing to limited sensor sensitivity, despite serving as the highest sensitivity that has ever been intraoperatively applied. Further studies should be conducted using sensors with higher sensitivity to detect vascular displacements below 0.72 μm in a sterile operative environment, which may improve the frequency profile of low displacement amplitude. Although this study followed the measuring technique established in our previous studies,[10] a mechanical arm with definite angulation may reduce the measurement bias due to the inconvenient intraoperative adjustment of angulation. Second, as time series analysis is less proficient at a high sampling rate, an interpolation algorithm was used to splice the time element of the displacement data; this can cause a limitation in the frequency analysis. Nevertheless, the currently implemented spectrotemporal results are close to the original 1000 μs sampling cycle, where the frequency of both vascular wall

displacement data is primarily below the hearing threshold. Thus, we consider this issue to be minor.

5. Conclusion

The time series method revealed a temporal correlation between the displacement of the vascular wall and the fluctuation of flow velocity. This finding provides fundamental evidence that the pulse-synchronous displacement of the sigmoid sinus vascular wall is temporally correlated with the syphoning of venous return. In this case, flow impact triggered an 11 μm peak displacement of the sigmoid sinus vascular wall once the osseous and vascular walls are separated. However, the correlation between the frequency of the forced vibration and the intravascular flow velocity fluctuation is insignificant, as indicated by the magnitude squared coherence method. Furthermore, the current sensed frequency of the sigmoid sinus vascular wall displacement is insufficient to cause audible noise. Thus, the production of vibroacoustic sounds may not be limited to the focal dehiscent area. Forced vibration in juxta-dehiscent areas may also induce vibroacoustic sound production; however, a further investigation is warranted.

Acknowledgments

This work was supported by NSFC No. 81670933 to Wuqing Wang. We thank Y.-D. Hsieh, MD for performing time series analysis and drafting the method and results in this study.

References

1. Z. Mu, X. Qiu, D. Zhao, X. Li, M. Fu, Y. Liu, B. Gao, P. Zhao and Z. Wang, *Comput. Methods Programs Biomed.* **190** (2020) 105373.
2. J. J. Song, G. S. An, I. Choi, D. De Ridder, S. Y. Kim, H. S. Choi, J. H. Park, B. Y. Choi, J. W. Koo and K. Lee, *Otol. Neurotol.* **37** (2016) 613.
3. G. S. Liu, B. C. Boursiquot, N. H. Blevins and Y. Vaisbuch, *Otolaryngol. Head Neck Surg.* **160** (2019) 749.
4. N. L. Kline, K. Angster, E. Archer, P. Raghavan, R. E. Morales, M. K. Mathews and D. J. Eisenman, *Am. J. Otolaryngol.* **41** (2020) 102675.
5. D. J. Eisenman, P. Raghavan, R. Hertzano and R. Morales, *Laryngoscope* **128** (2018) S1.
6. Y. L. Hsieh, X. Wang, X. Xu, Y. Wu, S. Wang, D. Yu, Y. C. Hsieh and W. Wang, *Sens. Mater.* **33** (2021) 3439.
7. Y. L. Hsieh, X. Xu, Y. Wu and W. Wang, *Laryngoscope Investig. Otolaryngol.* **6** (2021) 1436.
8. P. Zhao, H. Ding, H. Lv, X. Li, X. Qiu, R. Zeng, G. Wang, J. Wei, L. Jin, Z. Yang, S. Gong and Z. Wang, *Eur. Radiol.* **31** (2021) 2896.
9. X. Li, X. Qiu, H. Ding, H. Lv, P. Zhao, Z. Yang, S. Gong and Z. Wang, *J. Magn. Reson. Imaging* **53** (2021) 1744.
10. S. Huang, X. Li, X. Xue, X. Qiu, Z. Mu, M. Fu, B. Gao, P. Zhao and Z. Wang, *Med. Eng. Phys.* **86** (2020) 8.

11. Z. Mu, L. Liu, Y. Sun, B. Gao, H. Lv, P. Zhao, Y. Liu and Z. Wang, *Int. J. Numer. Method Biomed. Eng.* **37** (2021) e3526.
12. Z. Mu, Y. Sun, X. Li, X. Qiu, B. Gao, Y. Liu, P. Zhao and Z. Wang, *Biocybern. Biomed. Eng.* **41** (2021) 1197.
13. Y. L. Hsieh, X. Gao, X. Wang, F. C. Hsiang, X. Sun and W. Wang, *Front. Bioeng. Biotechnol.* **9** (2021) 777648.
14. Y. L. Hsieh and W. Wang, *Sens. Mater.* **33** (2021) 2013.
15. S. Tian, L. Wang, J. Yang, R. Mao, Z. Liu and Y. Fan, *J. Biomech.* **52** (2017) 68.
16. S. Tian, X. Fan, Y. Wang, Z. Liu and L. Wang, *J. Biomech.* **84** (2019) 197.
17. Y. L. Hsieh and W. Wang, *Otol. Neurotol.* **41** (2020) e132.
18. P. Guo and W. Q. Wang, *Clin. Exp. Otorhinolaryngol.* **8** (2015) 111.
19. K. Bhatnagar, A. T. Lataille and D. J. Eisenman, *Am. J. Otolaryngol.* **41** (2020) 102647.
20. Y. L. Hsieh, Y. Wu, H. Wang, X. Xu, P. Guo, X. Wang, Y. D. Hsieh, H. Lu and W. Wang, *ORL J. Otorhinolaryngol. Relat. Spec.* **84** (2022) 219.
21. S. N. Park, J. S. Han, J. M. Park, H. J. Jin, H. A. Joo, J. T. Park, J. Y. Koo, Y. Kim, M. Y. Kwak, J. W. Seo, C. I. Song and H. J. Park, *Clin. Otolaryngol.* **45** (2020) 280.
22. S. H. Kim, G. S. An, I. Choi, J. W. Koo, K. Lee and J. J. Song, *PLoS One* **11** (2016) e0157722.
23. K. Valluru, J. Parkhill, A. Gautam, H. Haraldsson, E. Kao, J. Leach, A. Wright, M. Ballweber, K. Meisel, D. Saloner and M. Amans, *Otol. Neurotol.* **41** (2020) e7.